A Robust Bad-Pixel Radiance Reconstruction for the Geostationary Environment Monitoring Spectrometer (GEMS) – Influences on Aerosol Retrieval

Heesung Chong, Won-Jin Lee, *Member, IEEE*, Hyung-Sup Jung, *Member, IEEE*, Yeseul Cho, Jhoon Kim, *Member, IEEE*, and Gonzalo González Abad

***Abstract*— The Geostationary Environment Monitoring Spectrometer (GEMS), launched in February 2020, performs hourly measurements of earthshine radiances to retrieve column amounts of air pollutants over Asia. However, the charge-coupled device detector of GEMS has bad pixels that exhibit abnormal radiometric responses, which translates to a decrease in the quality of radiance measurements. Permanent bad pixels result in an information gap in the aerosol product at ∼14.4°N–16.1°N latitudes (e.g., in Manila, the Philippines, and Mainland Southeast Asia), which cannot be filled even with long-term observations owing to the structure of the east–west scanning mechanism of GEMS. Here, we propose a robust method to reconstruct radiances measured inaccurately by the bad pixels, based on spectral correlation induced mainly by the Fraunhofer line structures. The reconstruction aims at the bad pixels in the wavelength range of ∼485–491 nm, which affects aerosol retrieval. We estimate that uncertainties in the reconstructed optical depths are ∼2 orders of magnitude smaller than typical aerosol optical depths. Our results demonstrate that the reconstructed radiances effectively restore the physical distributions of visible aerosol indices, improving the determination of aerosol types. Furthermore, the reconstructed radiances enhance retrievals of aerosol layer height (ALH), holding particular significance for the long-term accumulation of ALH data over Southeast Asia using GEMS.**

***Index Terms*— Aerosol retrieval, bad pixels, charge-coupled device (CCD) detector, data reconstruction, Geostationary Environment Monitoring Spectrometer (GEMS).**

I. Introduction

THE Geostationary Environment Monitoring Spectrometer (GEMS) is the world's first satellite-based hyperspectral ultraviolet–visible (UV–VIS) sensor operating from a geostationary orbit (GEO) [1], [2]. GEMS was launched in February 2020 onboard the Geostationary Korea Multi-Purpose Satellite 2B (GEO-KOMPSAT-2B, GK-2B), aiming to monitor air quality over Asia (5°S–45°N, 75°E–145°E) on an hourly basis. GEMS Level-2 baseline products provide physical quantities essential to assess air quality, including aerosol optical properties (AOPs), ultraviolet index (UVI), and column amounts of trace gases, such as ozone (O_3), nitrogen dioxide (NO_2), sulfur dioxide (SO_2), formaldehyde (HCHO), glyoxal (CHOCHO), and others.

These GEMS Level-2 products are derived by applying the state-of-the-art retrieval algorithms to earthshine radiance and solar irradiance spectra (i.e., Level-1 data), measured via a 2-D charge-coupled device (CCD) detector covering a spectral range of 300–500 nm. The GEMS CCD comprises 1032 (spectral) × 2048 (spatial) photoactive pixels; however, they contain "bad pixels," which cannot detect accurate signals due to sensor defects. Using radiance or irradiance values measured at these bad pixels hinders acquiring high-quality Level-2 products.

Bad (or missing) pixels are found not only in GEMS data but also in other satellite images. The information gaps induced by those pixels have motivated the development of methods to reconstruct Level-1 data from various spaceborne instruments, including the Moderate Resolution Imaging Spectroradiometer (MODIS) [3], [4], [5], [6], [7], [8], Landsat [4], [5], [6], [7], [8], [9], [10], [11], and Gaofen-1 [12].

Permanent bad pixels on the GEMS CCD have particularly significant impacts in terms of information gaps. This is because the instrument consistently uses the same detector pixels to view a specific location on the Earth's surface while scanning its domain in Asia from east to west every daylight hour. The zonal information gaps resulting from the bad pixels at specific latitude bands span the entire field of regard and cannot be filled even through long-term observations.

To fill these gaps, the operational GEMS Level-1 algorithm reconstructs the data by performing a 1-D linear interpolation

Manuscript received 28 May 2023; revised 9 October 2023 and 2 January 2024; accepted 30 January 2024. Date of publication 26 February 2024; date of current version 8 March 2024. This work was supported by the National Institute of Environmental Research (NIER), funded by the Korea Ministry of Environment (ME) of the Republic of Korea under Grant NIER-2023-01-01-086 and Grant NIER-2023-04-02-050. *(Corresponding author: Won-Jin Lee.)*

Heesung Chong is with the Department of Atmospheric Sciences, Yonsei University, Seoul 03722, South Korea, and also with the Center for Astrophysics | Harvard & Smithsonian, Cambridge, MA 02138 USA.

Won-Jin Lee is with the Environmental Satellite Center, Climate and Air Quality Research Department, National Institute of Environmental Research, Incheon 22689, South Korea (e-mail: wjleeleo@korea.kr).

Hyung-Sup Jung is with the Department of Geoinformatics, the University of Seoul, Seoul 02504, South Korea.

Yeseul Cho and Jhoon Kim are with the Department of Atmospheric Sciences, Yonsei University, Seoul 03722, South Korea.

Gonzalo González Abad is with the Center for Astrophysics | Harvard & Smithsonian, Cambridge, MA 02138 USA.

This article has supplementary material provided by the authors and color versions of one or more figures available at https://doi.org/10.1109/TGRS.2024.3369056.

Digital Object Identifier 10.1109/TGRS.2024.3369056

in the spatial (north–south) dimension of the CCD using the piecewise cubic Hermite interpolating polynomial (PCHIP) [13]. This approach is suitable for solar irradiance spectra, which are supposed to be spatially homogeneous for a fixed wavelength. However, the approach has a limitation when applied to earthshine radiances, whose values significantly vary in the spatial dimension depending on the optical properties of the atmosphere and the Earth's surface along the light paths.

For two reasons, it is rational to devise a novel approach for replacing radiances from the bad pixels on the GEMS CCD. First, the operational Level-1 algorithm already provides interpolated, not measured, radiances with significant errors. Second, replaced pixels can be flagged in data files so that users can choose whether to use them or not.

There are three prominent defect areas on the GEMS CCD [14], and this study focuses specifically on the one that affects radiance measurements in the spectral range of ∼485–491 nm at ∼14.4–16.1°N latitudes. Since this spectral range is used for retrieving AOPs from GEMS [15], [16], aerosol information is rendered permanently inaccurate in this latitude band, which covers a part of Metro Manila, the Philippines, suffering from severe black carbon pollution [17], [18], [19], and Mainland Southeast Asia, where significant aerosol emissions frequently occur from biomass burning during dry seasons [20], [21], [22].

GEMS AOP data comprise key parameters, including aerosol optical depth (AOD), single scattering albedo (SSA), and aerosol layer height (ALH). These data are spatially and temporally co-located with GEMS trace gas products, offering valuable insights for a comprehensive understanding of the interaction between aerosols and their precursors in Asia. In addition, GEMS AOP data play a critical role from a technical perspective, serving as essential inputs for other GEMS Level-2 algorithms [23], [24], [25].

The GEMS aerosol retrieval algorithm employs six channels, with the inclusion of a 490-nm channel primarily due to its high sensitivity to aerosol particle size. The 490-nm channel has also been chosen for intercomparison and synergetic applications with aerosol retrievals from the Second Geostationary Ocean Color Imager (GOCI-II) [26], [27]. The GOCI-II instrument is onboard the same satellite as GEMS and has a 490-nm channel, conducting hourly measurements in between GEMS scan hours for a 2500 km × 2500 km domain centered at 36°N and 130°E.

The current GEMS aerosol retrieval algorithm employs preconstructed lookup tables to achieve near-real-time (NRT) operation efficiency [15], [16], requiring a separate step to handle the bad pixels. The main objective of this study is to ensure that the NRT GEMS AOP retrievals at ∼14.4–16.1°N latitudes offer consistent data quality with other areas in the GEMS domain by reconstructing radiances measured by the bad CCD pixels. As the GEMS aerosol algorithm has been optimized for the use of the 490-nm channel, the radiance reconstruction can benefit the spatially consistent aerosol retrievals over the entire GEMS domain with minimal algorithmic changes.

Recently, machine-learning methods were suggested for spectral replacement as an alternative to the operational PCHIP interpolation of GEMS radiances [14]. While the machine-learning approach demonstrated high performance, consideration of additional computational costs for the NRT operation, resulting from the training process and the dependency on the input radiances, is yet to be addressed.

In this study, we propose a computationally efficient and robust method to fill the bad-pixel-driven gaps in GEMS radiance data. This method reconstructs the radiances using spectral correlation between measurements recorded by "good" CCD pixels at different wavelengths. The use of spectral information is the primary differentiator of our method compared to the currently operational algorithm that only applies the PCHIP in the spatial dimension. The spectral correlation is derived by simple linear regression, facilitating the NRT application. The proposed method is designed to use only two input files: irradiance and radiance from GEMS for a given day and hour.

The remainder of this article is organized as follows. Section II describes the proposed reconstruction method and the GEMS aerosol retrieval algorithm. Evaluations of the reconstructed GEMS radiances and the corresponding Level-2 data are presented in Section III. Finally, Section IV summarizes this study and delivers conclusions.

II. METHODOLOGY

A. GEMS Level-1 Data

GEMS conducts one solar irradiance and 6–10 earthshine radiance measurements daily for the 300–500-nm spectral range with ∼0.6-nm resolution and ∼0.2-nm sampling. Each solar irradiance data comprises a single image, while each earthshine radiance data typically comprises either 695, 313, or 347 images. Each image has 1033 (spectral) × 2048 (spatial) pixels, with one imaginary spectral grid added to the actual photoactive CCD pixel number (1032) for smooth interpolation between spectra from two separate CCD quadrants. During earthshine radiance measurements, a scanline is projected on the Earth's surface, aligning the 2048 spatial CCD pixels in the north–south direction. As GEMS conducts its step-and-stare scans from east to west, an image of 1033 × 2048 pixels is acquired from each scanline. Consequently, a hyperspectral radiance cube is generated by GEMS every hour, consisting of 1033 (spectral) × 2048 (spatial) × n (image) pixels, where n represents the number of east–west scanning steps (scanlines). The number of images in the radiance data (i.e., n) varies depending on the month and hour, which can be determined by uplink commands from the ground station (the maximum scanning step number is 695 for the current settings considering exposure time). The nominal spatial resolution is 3.5 km × 7.7 km over Seoul, South Korea.

In the operational GEMS image processing, bad pixels on the GEMS CCD are initially characterized as having radiometric responses significantly deviating from the average. Locations of these bad pixels were mapped prior to the launch. In addition, the operational GEMS Level-1 algorithm detects saturated pixels in real time and reports them as bad pixels.

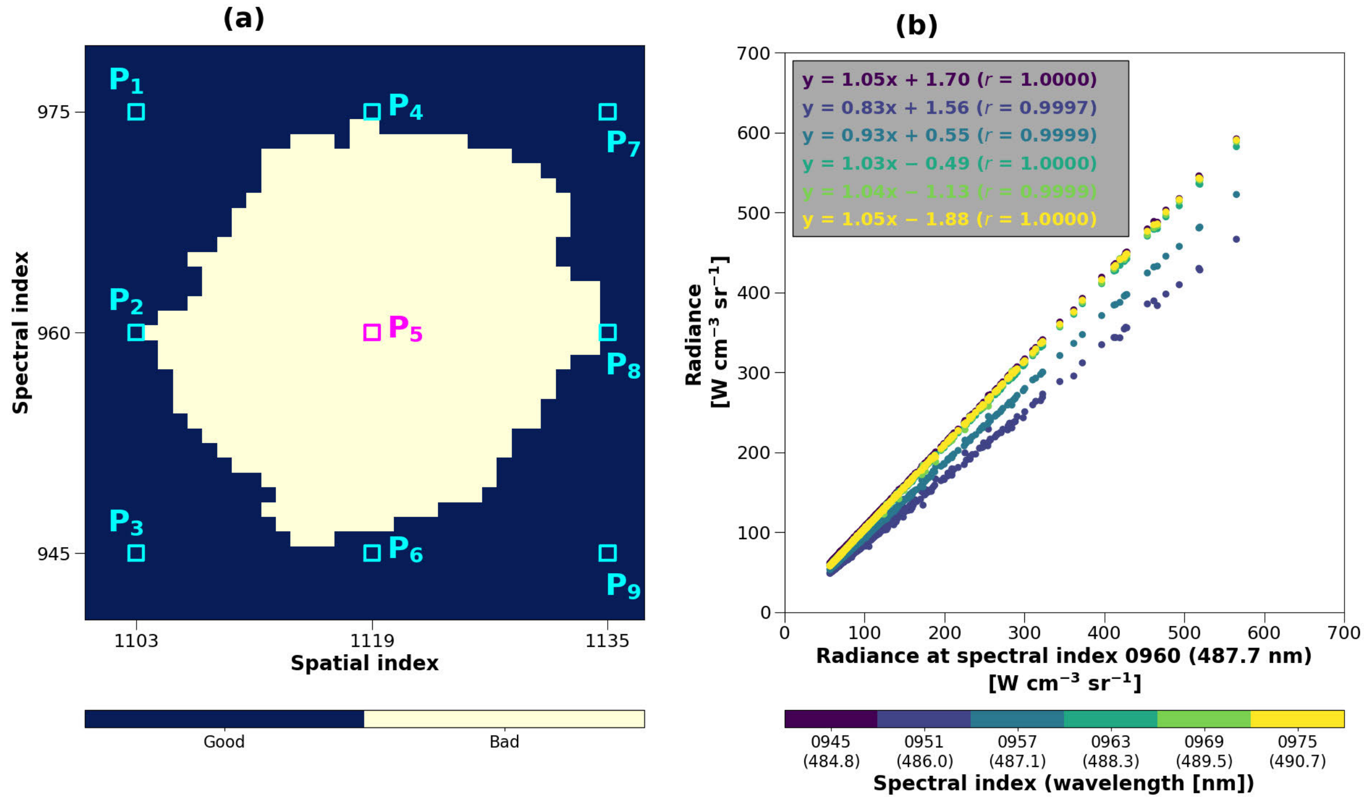

Fig. 1. Fundamental principle of bad pixel reconstruction. (a) Map of the bad pixel cluster (BPC) of interest. P_5 represents the pixel to be reconstructed, while other marked pixels represent good pixels used in the bad-pixel radiance reconstruction. (b) Linear relationships between radiances from pairs of good spectral indices around the BPC. A spatial index of 1103 is selected. Each spectral index is denoted by a specific color, along with its corresponding wavelength. The number of data points on each scatter plot corresponds to the number of scanlines (695 in all these examples). A linear regression equation and its corresponding correlation coefficient are indicated for each scatter plot. The radiances in (b) were measured by GEMS at 03:45–04:15 UTC on April 1, 2021.

Accordingly, the final bad pixel mask (BPM) arrays of the GEMS Level-1 data have the same dimensions as the measurement arrays (i.e., 1033 × 2048 for irradiance and 1033 × 2048 × n for radiance), having only two types of binarized elements: 1 for bad and 0 for good pixels. Often, a single-scanline radiance image has more bad pixels than irradiance, mainly due to saturation in cloudy scenes. Saturated pixels in irradiance data are unlikely because the instrument uses different exposure settings for solar measurements, involving a diffuser with transmittances <30% at a 30° incident angle. This study aims to reconstruct radiance spectra measured by bad but not saturated pixels. Therefore, this study uses the BPM arrays from the solar irradiance dataset to identify the locations of bad pixels on a daily basis.

The GEMS CCD exhibits three prominent defect areas characterized by bad pixels [14]. The first defect area spans a broad spectral range of ~400–500 nm but occupies only three pixels in the spatial dimension, projecting onto a latitude band of ~0.3–0.4°N in radiance data. Another defect area affects radiance qualities within the wavelength range of ~300–400 nm for ~11.9–12.9°N latitudes. This study focuses specifically on the bad pixels within the third defect area, which corresponds to spatial indices of 1104–1134 and spectral indices of 946–974 (all indices in this study are 0-based). A graphical representation of this circle-shaped "bad pixel cluster (BPC)" on the CCD is presented in Fig. 1(a). As previously mentioned, the wavelength and latitude ranges associated with this BPC are approximately 485–491 nm and 14.4–16.1°N, respectively. More detailed descriptions of the first two defect areas can be found in [14].

B. Spectral Correlation in Radiances

An earthshine radiance I measured by the sensor at wavelength λ represents sunlight backscattered from the Earth's atmosphere and surface. Based on the Beer–Lambert law, $I(\lambda)$ can be theoretically expressed as

$$I(\lambda) = \left(\tilde{I}_0(\lambda)\exp\left[-\tilde{\tau}(\lambda)\right]\right) \otimes \Gamma(\lambda', \lambda) + C(\lambda) \quad (1)$$

which characterizes: 1) the attenuation of sunlight by the atmosphere and surface; 2) the distortion of spectral lines due to the finite bandpass of the spectrometer; and 3) radiometric errors. The parameters $\tilde{I}_0$ and $\tilde{\tau}$ represent the solar irradiance and atmospheric/surface attenuation optical depth, respectively, at infinitely high spectral resolution. The symbol $\otimes$ represents the convolution operator, with $\Gamma(\lambda', \lambda)$ describing the spectral response function that characterizes the instrument's response at wavelength λ to signals from wavelength λ'. The term $C(\lambda)$ accounts for radiometric errors resulting from imperfect instrumental calibration and characterization. For practical purposes, the convolution can be applied separately to the solar irradiance term and the optical depth term by accounting for the solar I_0 effect [28]

$$I(\lambda) = I_0(\lambda)\exp[-\tau(\lambda)] \tag{2}$$

where I_0 and τ represent the convolved solar irradiance and optical depth, respectively. Here, τ illustrates the combined effects of every factor contributing to the difference between $I_0(\lambda)$ and $I(\lambda)$, including geophysical processes in the Earth's atmosphere and at the surface, instrumental effects [i.e., $C(\lambda)$], and the solar I_0 effect.

Therefore, the spectral structures of I originate from those of I_0 and τ. The spectral structures identified in I_0 are referred to as the Fraunhofer lines [29]. These lines result from the absorption of light by chemical elements present in the solar atmosphere and thus are consistently found in every solar spectrum. In fact, a spectral calibration algorithm for GEMS leverages these persistent Fraunhofer lines to detect wavelength shifts in measured solar irradiance data through cross-correlation with a high-resolution solar reference spectrum [30].

For two arbitrary wavelengths λ_1 and λ_2 within the GEMS spectral coverage, a ratio (a) between convolved irradiance values $I_0(\lambda_1)$ and $I_0(\lambda_2)$ can be calculated from a single spectrum, representing the linear relationship driven by the Fraunhofer lines

$$I_0(\lambda_2) = aI_0(\lambda_1). \tag{3}$$

Combining (2) and (3) leads to the following equation:

$$I(\lambda_2) = aI(\lambda_1)\exp[\tau(\lambda_1) - \tau(\lambda_2)] \tag{4}$$

which finally represents the linear relationship between the radiances at wavelengths λ_1 and λ_2. This equation indicates that the relationship is determined by two factors: 1) the ratio a from the solar Fraunhofer lines and 2) the optical depth difference between the two wavelengths [i.e., $\tau(\lambda_1) - \tau(\lambda_2)$].

The spectral structures in τ result from various factors, including trace gas absorption, Raman scattering, aerosol scattering/absorption, Rayleigh scattering, wavelength-dependent surface albedos, and unresolved instrument calibration. In UV–VIS trace gas retrieval algorithms, the spectral structures of these factors except the trace gas absorption and Raman scattering are often approximated by polynomials, taking advantage of their smoothly varying features [31], [32]. Given the narrow wavelength range marked by the bad CCD pixels of interest in this study (~485–491 nm), the optical depth variations by wavelength are expected to be small for those factors having smooth spectral features. Besides, within this wavelength range, it is common for the optical depths of trace gases to exhibit spectral variations typically on the order of 10^{-3} [33]. (The dominant contributors to trace gas optical depths in this range are O_3 and the oxygen collision-induced absorption, i.e., O_2–O_2.) Considering that $|\tau(\lambda_1) - \tau(\lambda_2)|$ is expected to be significantly smaller than 1, it is reasonable to approximate the optical-depth-related term in (4) using the first-order Taylor series expansion as follows:

$$\begin{aligned} I(\lambda_2) &\approx aI(\lambda_1)[1 + \tau(\lambda_1) - \tau(\lambda_2)] \\ &= aI(\lambda_1) + b \end{aligned} \tag{5}$$

where b is an additive term to represent $aI(\lambda_1)[\tau(\lambda_1)-\tau(\lambda_2)]$.

The idea for the radiance reconstruction in this study is to derive the parameters a and b in (5) using only good CCD pixels and apply them to determine radiances for the bad pixels. The basic premise of this approach is that a consistent spectral relationship can be found in radiances measured from different locations on the Earth's surface within a narrow wavelength range of around 485–491 nm. In practice, however, the spectral relationships observed from different locations are hardly identical. Of the two factors that determine the relationship mentioned above, the Fraunhofer structures are globally consistent for a given day. In contrast, the spectral patterns of optical depths exhibit location-dependent variations attributed to dissimilar atmospheric and surface properties. These variations are the major error sources of the reconstruction method in this study. However, as our goal is to facilitate the GEMS AOP retrieval, pursuing the reconstruction is worthwhile as long as the errors remain small enough to retrieve AODs with reliable qualities. The errors in reconstructed radiances are estimated in Section III-A, following the detailed descriptions of the reconstruction method and the aerosol retrieval algorithm in Sections II-C and II-D, respectively.

Fig. 1(b) demonstrates the spectral correlations between radiances measured at different wavelengths around the BPC at 03:45–04:15 UTC on April 1, 2021. All 695 scanlines in the east–west dimension are used to analyze the correlations. The x-axis of Fig. 1(b) shows the radiance measurements from spectral index 960 (arbitrarily chosen within the BPC spectral range) and spatial index 1103, corresponding to CCD pixel P_2 in Fig. 1(a). The y-axis indicates the radiances from CCD pixels P_1 and P_3 in Fig. 1(a) and four others in spatial column 1103 (spectral indices of 951, 957, 963, and 969, arbitrarily chosen). Each scatter plot depicts an apparent linear relationship between two different wavelengths. The regression equations presented are derived following (5). Overall, the relationship is highly consistent despite the spatial variations in optical depths, indicating the dominant influence of the Fraunhofer ratio (a) over the optical depth contribution. Indeed, the Fraunhofer ratios calculated using GEMS-measured solar irradiances for the same condition given in Fig. 1(b) are 1.06, 0.84, 0.93, 1.04, 1.04, and 1.05 in ascending order of their spectral indices, almost identical to the slopes of regression lines for radiances. According to (5), the y-intercepts of the regressions in Fig. 1(b) represent $aI(\lambda_1)[\tau(\lambda_1)-\tau(\lambda_2)]$. Given that the $aI(\lambda_1)$ values typically on the order of 10^2 [see Fig. 1(b)], the y-intercepts suggest that the optical depths differ at the 10^{-2} scale between two wavelengths around 485–491 nm (i.e., $|\tau(\lambda_1) - \tau(\lambda_2)| \sim 10^{-2}$). As described earlier, the location-dependent variations in $[\tau(\lambda_1) - \tau(\lambda_2)]$ lead to errors in the reconstructed radiances in this study, which is discussed in detail in Section III-A.

C. Reconstruction Method

The radiance reconstruction is performed on an hourly basis for each Earth scan. After identifying the BPC using the daily solar irradiance file, good-pixel radiance measurements are extracted around the BPC to derive the spectral relationships.

To minimize the spectral variations in optical depths, we restrict the wavelength range involved in the reconstruction by using only the good CCD pixels closest to the bad pixels in the spectral dimension [see Fig. 1(a)]. All wavelengths involved in the reconstruction are within a ~6-nm spectral window [see Fig. 1(b)].

The method we propose in this study involves eight good pixels to restore radiance at one bad pixel. For example, let pixel P_5 in Fig. 1(a) be the target for radiance reconstruction. We first find two good pixels that are closest to the outermost boundary of the BPC and have the same spatial index as P_5, i.e., P_4 (spectral index 975) and P_6 (spectral index 945). Then, pixels P_2 and P_8 are selected via the same approach, but with the spatial and spectral axes exchanged. Finally, we choose pixels P_1, P_3, P_7, and P_9, whose locations are determined through cross-combinations of the spatial and spectral indices of P_2, P_4, P_6, and P_8.

The objective of gathering these eight good pixels is to build the linear relationships in radiances between the target spectral index and the two reference indices, i.e., 975 and 945. Here, the spectral indices 975 and 945 represent the wavelengths of 490.7 and 484.8 nm, respectively, with the target spectral index falling in between. In the linear formula defined in (5), the two wavelength variables can be substituted with two spectral indices, one being the target and the other a reference.

First, the relationship between the target and spectral index 975 is derived by

$$\begin{bmatrix} \boldsymbol{x}_2^T \\ \boldsymbol{x}_8^T \end{bmatrix} = a_1 \times \begin{bmatrix} \boldsymbol{x}_1^T \\ \boldsymbol{x}_7^T \end{bmatrix} + b_1 + E_1 \tag{6}$$

where $\boldsymbol{x}_1$, $\boldsymbol{x}_2$, $\boldsymbol{x}_7$, and $\boldsymbol{x}_8$ are the vectors composed of radiances measured at P_1, P_2, P_7, and P_8, respectively. The elements in each vector are sorted in ascending order of the image indices (i.e., from east to west), with the total number of elements corresponding to that of scanlines. The coefficients a_1 and b_1 are derived through linear regression, representing the resultant spectral relationship. The residuals of the regression are described by E_1. Here, we assume that two different spatial CCD indices in (6) exhibit the same spectral and radiometric characteristics; however, in practice, the instrumental effects can differ by CCD pixels, and the potential errors caused by these differences are accounted for by E_1.

The second coefficient set of a_2 and b_2, accounting for the relationship between the target and spectral index 945, is calculated using the same equation structure as (6), but with radiances measured at P_3 and P_9 ($\boldsymbol{x}_3$ and $\boldsymbol{x}_9$) and the corresponding residuals E_2 on the right-hand side

$$\begin{bmatrix} \boldsymbol{x}_2^T \\ \boldsymbol{x}_8^T \end{bmatrix} = a_2 \times \begin{bmatrix} \boldsymbol{x}_3^T \\ \boldsymbol{x}_9^T \end{bmatrix} + b_2 + E_2. \tag{7}$$

The two sets of linear regression coefficients obtained from (6) and (7) lead to two different calculations for reconstructing radiances at P_5

$$\boldsymbol{x}_{5,1} = a_1 \times \boldsymbol{x}_4 + b_1 \tag{8}$$

and

$$\boldsymbol{x}_{5,2} = a_2 \times \boldsymbol{x}_6 + b_2 \tag{9}$$

where $\boldsymbol{x}_{5,1}$ and $\boldsymbol{x}_{5,2}$ represent radiances constructed using measurements from spectral indices 975 and 945, respectively. By combining the two reconstructions, the final estimates for radiances at P_5 ($\boldsymbol{x}_5$) are derived as follows:

$$\boldsymbol{x}_5 = \boldsymbol{x}_{5,1} \times \frac{1/r_1}{(1/r_1 + 1/r_2)} + \boldsymbol{x}_{5,2} \times \frac{1/r_2}{(1/r_1 + 1/r_2)} \tag{10}$$

where r_1 and r_2 are relative (percentage) root-mean-square error (RMSE) values from the linear regressions in (6) and (7), respectively. Using the inverse of RMSE in (10) allows $\boldsymbol{x}_5$ to be calculated with a larger weighting for a more reliable vector between $\boldsymbol{x}_{5,1}$ and $\boldsymbol{x}_{5,2}$.

The same calculations are repeated with different P_5 positions until the reconstruction is completed for every bad pixel within the boundary of the BPC [see Fig. 1(a)]. The positions of P_2, P_4, P_6, and P_8 change depending on the position of P_5, while P_1, P_3, P_7, and P_9 are fixed.

D. GEMS Aerosol Retrieval Algorithm

The GEMS aerosol product provides hourly retrievals of AOPs over Asia in NRT. The corresponding data and image files can be found on the GEMS website operated by the National Institute of Environmental Research (NIER) (https://nesc.nier.go.kr/en/html/cntnts/91/static/page.do). Here, we briefly describe the GEMS aerosol retrieval algorithm and introduce how the bad pixels can influence the retrieved quantities. The detailed descriptions of the aerosol retrieval algorithm can be found elsewhere [15], [16], [34], [35].

The final outputs of the GEMS aerosol retrieval algorithm are AOD, SSA, and ALH. To derive these quantities, the algorithm uses radiance and irradiance measurements at six wavelengths: 354, 388, 412, 443, 477, and 490 nm. These wavelengths were selected to avoid significant trace gas absorption, with the exception of 477 nm, which is sensitive to O_2–O_2 absorption and thus beneficial for determining ALH values [34]. To enhance the signals, radiance measurements within ±2.2 nm from each of the six wavelengths are averaged before retrieval.

The accuracy of the retrieved quantities depends on the accuracy of aerosol type determination. The GEMS algorithm classifies aerosols into: 1) highly absorbing fine (HAF); 2) dust; and 3) nonabsorbing (NA) types. The type determination is conducted using two intermediate quantities named ultraviolet aerosol index (UVAI) and visible aerosol index (VISAI). The UVAI and VISAI are calculated using wavelength pairs of 354/388 and 477/490 nm, respectively.

After the type determination, AOD and SSA at 443 nm are retrieved initially using normalized radiances at 354 and 388 nm [36]. These initial values of AOD and SSA are used for a priori states of an inversion using the optimal estimation method (OEM) [37], along with a measurement vector composed of Sun-normalized radiances at 354, 388, 412, 443, 477, and 490 nm. The outputs of the inversion correspond to AOD and SSA at 443 nm and ALH.

The aerosol retrieval from GEMS using the six selected channels offers a degree of freedom for signal of <2 for the three states (AOD, SSA, and ALH) [15], [16]. Therefore, the OEM-based inversion is designed to constrain AOD and SSA

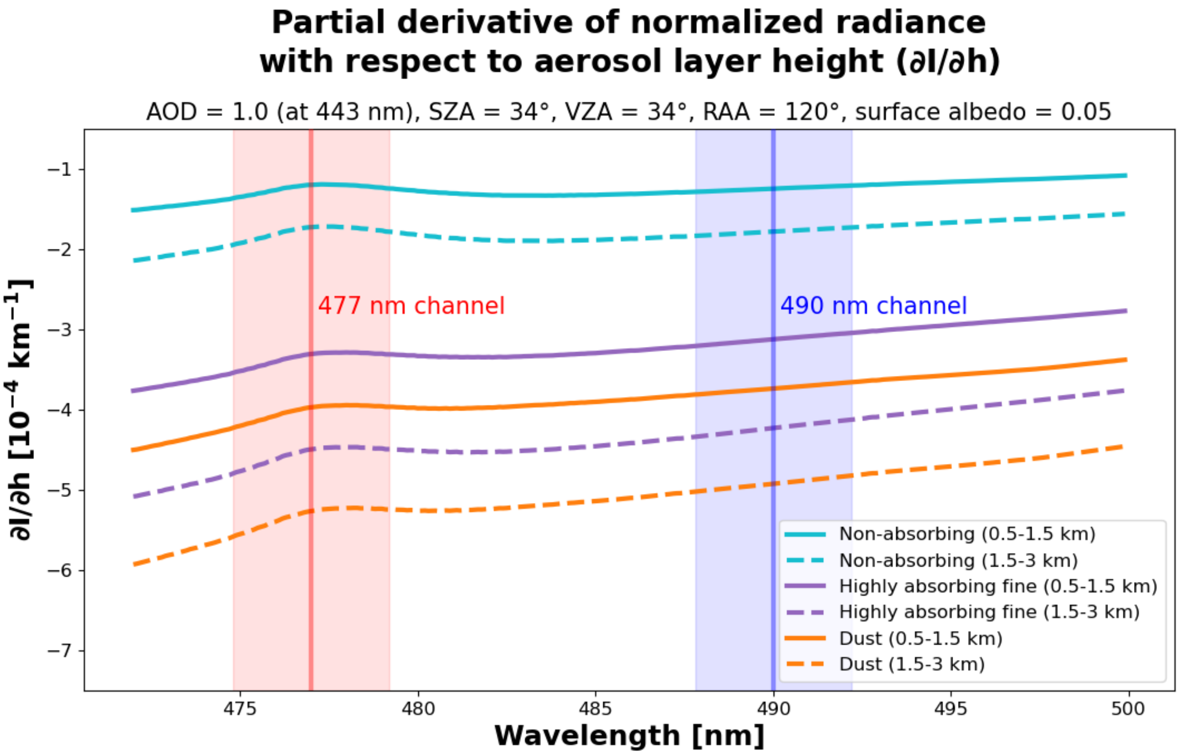

Fig. 2. Partial derivatives of normalized radiances with respect to ALH, calculated employing the VLIDORT model. ALH values of 0.5, 1.5, and 3 km are used for the calculations. Different aerosol types are indicated with different colors. Other input values for VLIDORT are indicated above the panel, including the SZA, VZA, and relative azimuth angle (RAA). The shades indicate ±2.2-nm wavelength windows where spectral binning is performed to enhance the signals.

strongly to the a priori states retrieved using 354 and 388 nm for the successful retrieval of ALH.

Among the six wavelengths employed for aerosol retrieval, the BPC considered in this study impacts the quality of measurements in the 490-nm channel. The intermediate retrieved quantities influenced are VISAI and aerosol types. Of the three ultimate outputs, AOD is minimally affected by the BPC, primarily when aerosol types are incorrectly determined due to VISAI errors, owing to the strong constraints in the OEM inversion. Retrieving SSA, representing the absorptivity of aerosols, is most sensitive to measurements at UV wavelengths [38]. Consequently, ALH is the most sensitive retrieved state to the quality of radiances at 490 nm.

Fig. 2 shows the partial derivatives of normalized radiances with respect to ALH, calculated using the Vector Linearized Discrete Ordinate Radiative Transfer (VLIDORT) model [39]. For the selected condition of AOD, observation geometries, and surface albedo, the partial derivatives exhibit negative values, indicating that an increase in ALH leads the aerosols to shield more photons scattered below their layer from reaching the sensor. In the 477-nm channel, bumps are found in the partial derivatives as an increase in ALH leads to a decrease in the extent of O_2–O_2 absorption below the aerosol layer [40], [41]. The partial derivatives show persistent values up to 490 nm with only small increases, implying that the quality deterioration of radiance measurements at 490 nm would affect the ALH retrieval.

To assess the impact of radiance reconstruction, we establish three target quantities: VISAI, aerosol types, and ALH. A target latitude band of the assessment is ∼14.4–16.1°N, which corresponds to the projection of the BPC onto the Earth's surface. The assessment results are presented in Section III-B.

III. EXPERIMENTAL RESULTS AND ANALYSIS

A. Radiance Reconstructions

Fig. 3 presents the reconstruction result using radiances from 03:45 to 04:15 UTC on April 1, 2021. A combination of spatial index 1119 and image index 500 is selected as an example. The radiance spectra before and after reconstruction exhibit significant differences at spectral indices 947–974 (485.2–490.5 nm), which correspond to the bad pixel coverage at spatial index 1119 [see Fig. 1(a)]. The solar irradiance spectrum from an adjacent good spatial index (1103) exhibits a consistent spectral pattern with the reconstructed radiance, demonstrating the dominant contribution of the Fraunhofer line structures, as described in Section II-B.

We perform a quantitative evaluation of the accuracy and precision of the reconstructed radiances by generating imaginary bad pixels (IBPs). The IBPs are constructed by simply replicating the BPC in Fig. 1(a) onto good pixels along the spatial dimension of the CCD, with its shape and size preserved [i.e., the BPC is translated along the *y*-axis in Fig. 4(a)]. Replicating the BPC means changing the BPM values for good pixels from 0 to 1 so that the reconstruction algorithm identifies them as bad pixels. Since these IBPs were originally good pixels, the pre-reconstruction measurements of radiances can be used as references for the evaluation.

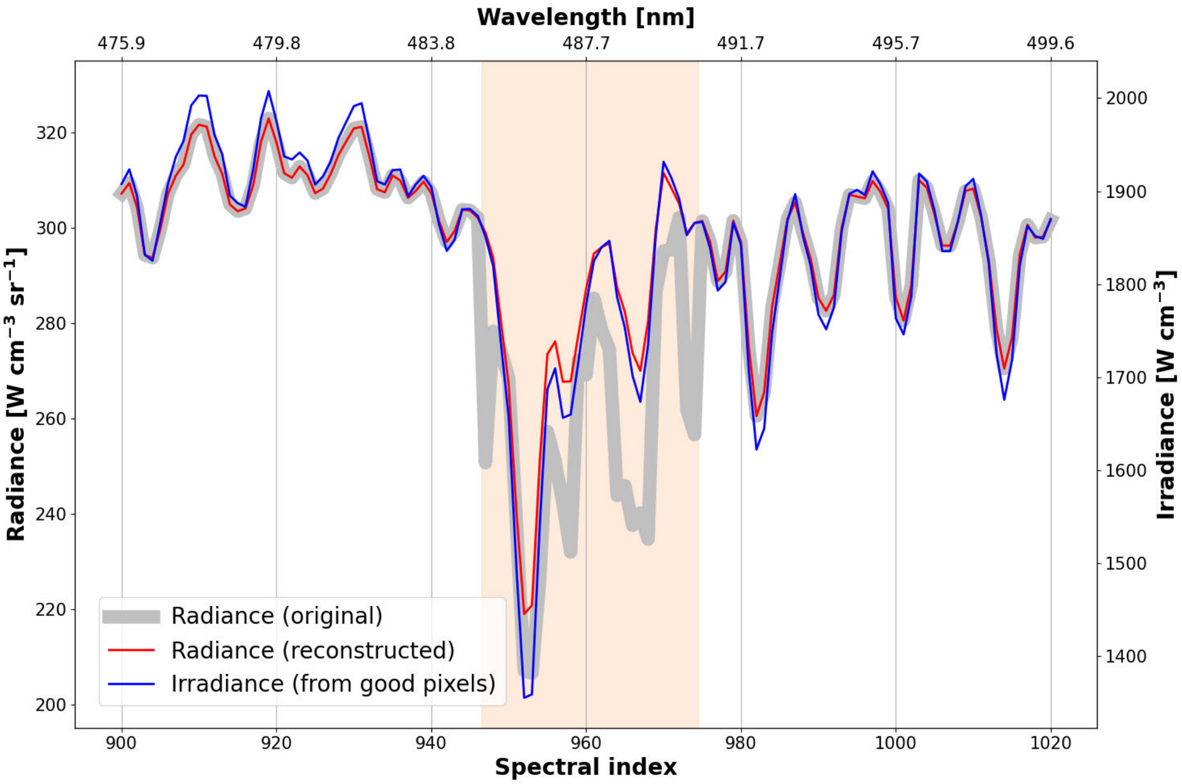

Fig. 3. Result of reconstruction using radiances from 03:45 to 04:15 UTC on April 1, 2021. Original and reconstructed radiances are presented for spatial index 1119 and image index 500. The solar irradiance spectrum for spatial index 1103 from April 1, 2021 is overplotted on a different y-axis range. The orange shade represents the bad pixel coverage at spatial index 1119 (spectral indices 947–974).

As mentioned earlier, errors in the reconstructions depend on the spatial variability in spectral patterns of optical depths. To assess the reconstruction performance for various levels of spatial variability, we use radiance measurements from 03:45 to 04:15 UTC on April 1, 2021, when cloud cover patterns were spatially heterogeneous across the field of regard [see Fig. 4(a)]. We generate the IBPs at two distant positions in the CCD. Hereafter, the position that measured fewer cloudy pixels is referred to as “clear” and the other as “cloudy.” The positions of IBPs (both clear and cloudy) are presented in Fig. 4, along with those of the BPC.

Fig. 4(b) and (c) shows the evaluation results for the clear and cloudy conditions, respectively. The x-axis of each panel represents the references measured originally by the IBPs, and the y-axis shows the reconstructed radiances. The spatial and spectral indices of the IBPs are fixed for the entire east–west scan, making the number of data points on each scatter plot 597 (number of bad CCD pixels) × 695 (number of scanlines). Values of the mean absolute error (MAE) and RMSE are calculated to represent the accuracy and precision, respectively. The agreements between measurements and reconstructions are excellent for both clear and cloudy cases, with high determination coefficients (R^2; both 0.9999) and low values of RMSE (0.35% and 0.46%) and MAE (0.23% and 0.26%).

To evaluate the robustness of the reconstruction method, we extend the temporal coverage of the IBP experiment to span one year (from August 2020 to July 2021) and incorporate data from three different hours (00:45–01:45, 03:45–04:15, and 06:45–07:15 UTC). Here, we construct IBPs at both spatial index ranges from Fig. 4(b) and (c) (870–900 and 514–544) for each scan regardless of cloudiness. Fig. 4(d)–(f) displays the results, demonstrating the robustness of the method proposed in this study in reconstructing radiances across various months and hours ($R^2 = 0.9999$, RMSE = 0.62%–0.80%, and MAE = 0.35%–0.40%).

Based on the definition of optical depth $\tau = -\ln(I/I_0)$, the uncertainties in reconstructed radiances can be converted to those in optical depths by the following propagation:

$$\varepsilon_\tau = \left|\frac{\varepsilon_I}{I}\right| \tag{11}$$

where ε_τ indicates the optical depth uncertainty and ε_I represents the radiance uncertainty. Substituting the relative RMSE values (0.62%–0.80%) for the right-hand side of (11) leads to ε_τ of 6.2–8.0 × 10^{-3}. These uncertainty magnitudes are comparable to typical optical depths of trace gases but ~2 orders of magnitude smaller than those of aerosols in the spectral range of interest [1], [33].

To further evaluate the reconstructed bad-pixel Fraunhofer lines, we compare the spectral structures with those from radiances measured by the Tropospheric Monitoring Instrument (TROPOMI), a low-Earth-orbit (LEO) hyperspectral spectrometer that has recorded earthshine spectra daily at 13:30 local time since October 2017 onboard the Sentinel-5 Precursor satellite [42]. Band 4 of the TROPOMI instrument (S5P_L1B_RA_BD4_HiR product) covers 405–500 nm [43], which encompasses the spectral range of the GEMS BPC. The

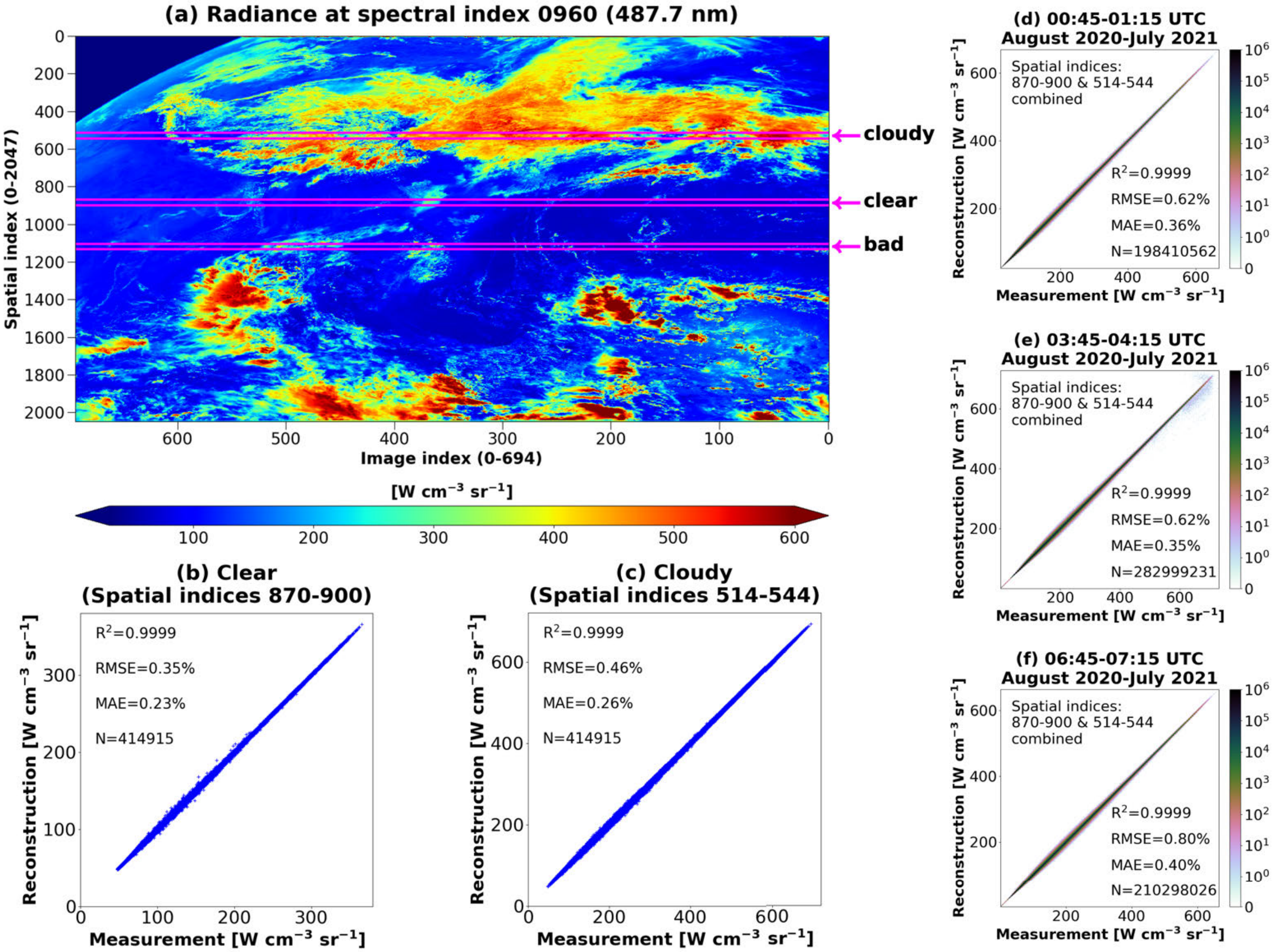

Fig. 4. Evaluation of the reconstructed radiances. (a) Map of radiances measured at spectral index 960 from 03:45 to 04:15 UTC on April 1, 2021. Spatial indices of IBPs are presented with magenta boxes and arrows for both clear (870–900) and cloudy (514–544) cases. See text for the definitions of "clear" and "cloudy." The spatial indices of the BPC are also indicated as "bad." The evaluation results for 03:45–04:15 UTC on April 1, 2021, are presented for the (b) clear and (c) cloudy cases with corresponding values of determination coefficient (R^2), RMSE, MAE, and the number of data points (N). (d)–(f) Evaluation results for 00:45–01:15, 03:45–04:15, and 06:45–07:15 UTC from August 2020 to July 2021, respectively. The two spatial index ranges in panels (b) and (c) are combined for the annual evaluations shown in (d)–(f).

spectral resolution and sampling of this TROPOMI band are 0.55 and 0.2 nm, respectively, comparable to those of GEMS.

Intercomparison between radiance measurements from LEO and GEO instruments needs to be carefully performed over a stable target, e.g., the deep convective cloud (DCC), with observation geometries matched [44]. However, it is challenging to co-locate TROPOMI and GEMS measurements over the latitudes in ~14.4–16.1°N, the region where the GEMS BPC is spatially projected while focusing only on stable targets. Therefore, here we assess only the correlation between the Fraunhofer structures in the TROPOMI and reconstructed GEMS radiance spectra, rather than comparing absolute radiance values.

We use four months of TROPOMI and GEMS data from October 2020, January 2021, April 2021, and July 2021 for the assessment to cover all four seasons. The spatial resolution of TROPOMI has changed since August 2019, and it is 5.5 km × 3.5 km for the period of interest in this intercomparison. For the co-location of the two data, we first create grid cells at 0.1° × 0.1° resolution for 14–16°N and 97–110° E, the area in Mainland Southeast Asia where the GEMS radiance measurements are conducted mostly via the bad pixels. Then, we calculate gridded mean values of solar zenith angles (SZAs), viewing zenith angles (VZAs), and radiances for every TROPOMI orbit that overpassed this area in the four selected months. For the adequate averaging and comparison of radiances, we perform spline interpolation of TROPOMI spectra onto the nominal GEMS wavelength grids before averaging. To produce gridded GEMS data, we search for scans conducted over the same area within 30 min before and after the TROPOMI measurements and apply the same averaging approach as TROPOMI to GEMS SZAs, VZAs, and radiances from spatial indices 1114–1122. This spatial index range corresponds to the center part of the BPC where the most significant loss of spectral information occurs [see Fig. 1(a)]. The GEMS gridded mean values are calculated

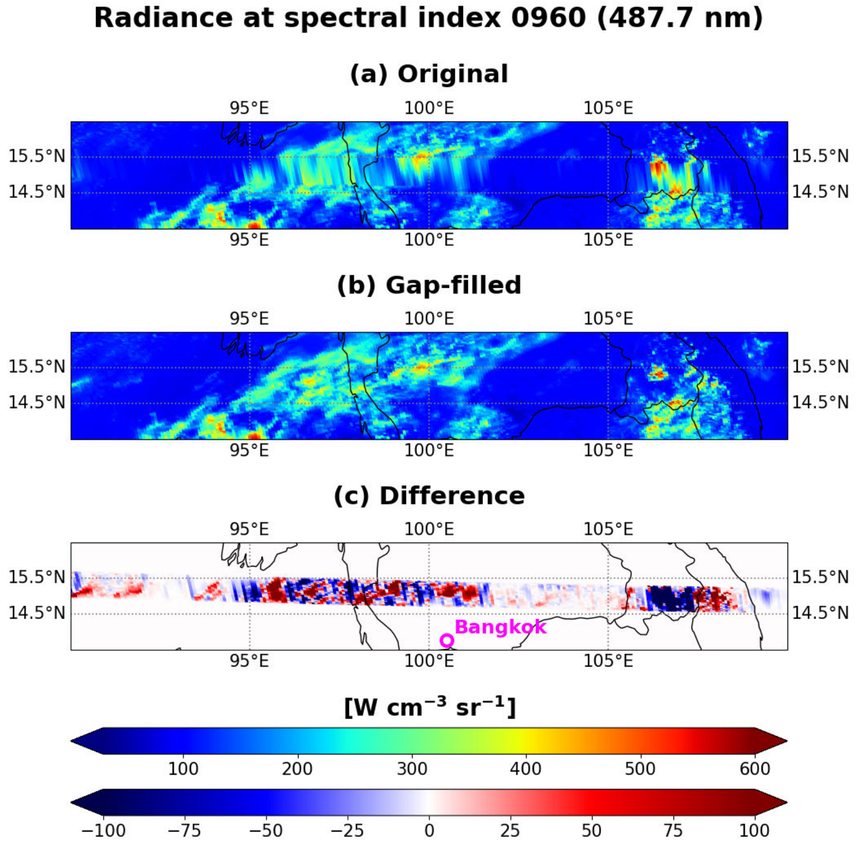

Fig. 5. Comparison between the original and reconstructed radiances for 03:45–04:15 UTC on April 1, 2021. The respective panels present: (a) original radiances from the operational algorithm; (b) gap-filled radiances (i.e., reconstructed radiances are presented for bad pixels); and (c) differences between gap-filled and original radiances [i.e., (b)–(a)]. The selected spectral index is indicated.

for both data before and after radiance reconstruction. Finally, we discard all gridded data of TROPOMI and GEMS, except for those exhibiting SZA and VZA differences between the two instruments of less than 1°. As a result, we obtain a total of 299 sample pairs to compare.

After the co-location, we produce scaled radiances by dividing each of the TROPOMI and GEMS spectra by the radiance value from spectral index 895 (474.9 nm). Fig. S1(a) in the Supplementary Material shows the mean scaled radiances of TROPOMI and GEMS for both before and after reconstruction. The Fraunhofer structures in the reconstructed GEMS radiances are consistent with those in the mean TROPOMI spectrum, while the mean GEMS spectrum before reconstruction exhibits a significant discrepancy.

We calculate correlation coefficients (r) between the scaled GEMS and TROPOMI spectra for each of the 299 samples within the spectral indices 948–972 (485.4–490.1 nm) [see Fig. S1(b) in the Supplementary Material]. The reconstructed GEMS spectra exhibit r values close to unity (0.9926 on average), indicating the successful reproduction of the Fraunhofer lines, while the GEMS spectra before reconstruction show lower and variable r values with the mean and standard deviation of 0.56 and 0.34, respectively.

Fig. 5 presents a comparison between original and reconstructed (gap-filled) radiances for 03:45–04:15 UTC on April 1, 2021. Without reconstruction [see Fig. 5(a)], the radiance data from the operational algorithm have artifactual spatial features at latitudes around 14.4–16.1°N. The radiance values in this latitude band show elongated patterns in the north–south direction, revealing the limitation of the operational 1-D linear interpolation (PCHIP). In contrast, the reconstruction approach proposed in this study can rebuild the physical distributions of radiances [see Fig. 5(b)]. The realistic cloud distribution at the latitude band 14.4–16.1°N in Fig. 5(b) demonstrates the effectiveness of the proposed reconstruction. The differences between the reconstructed and original radiances range from –404.4 to +353.9 W cm^{-3} [see Fig. 5(c)]. Percentage differences are from –81.9% to +394.8%, sufficiently large to impact Level-2 retrievals.

B. Effects on the Aerosol Product

Fig. 6(a) and (c) depicts the original VISAI distributions derived without radiance reconstruction for two different longitude ranges for a scan at 04:45–05:15 UTC on April 1, 2021. A zonal band with values noticeably distinct from its surroundings appears at latitudes around 14.4–16.1°N, indicating significant anomalies in VISAI due to errors in radiance interpolation by the operational PCHIP algorithm. Fig. 6(a) and (c) illustrates how the BPC hinders the continuous monitoring of urban-scale air quality across Southeast Asia, including Myanmar, Thailand, Laos, Vietnam, and the Philippines. For example, the band-shaped anomaly of VISAI crosses the

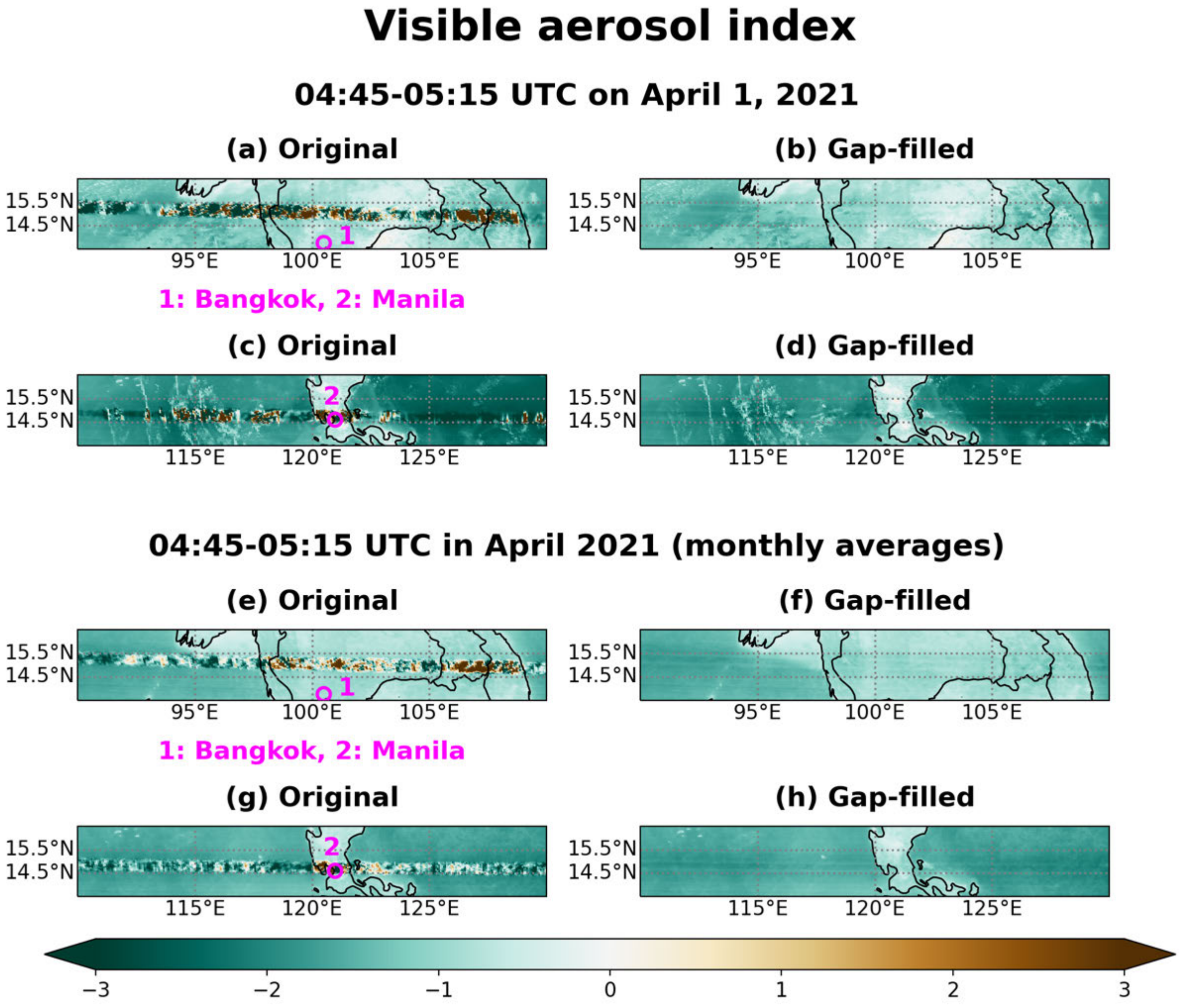

Fig. 6. Comparisons of visible aerosol indices (VISAIs) retrieved from GEMS using original and gap-filled radiances. (a)–(d) 1-h comparison for 04:45–05:15 UTC on April 1, 2021, while (e)–(h) compare monthly mean VISAIs for 04:45–05:15 UTC in April 2021. Two different longitude ranges are presented: (a), (b), (e), and (f) 90–110° E and (c), (d), (g), and (h) 110–130° E. The locations of Bangkok, Thailand, and Manila, the Philippines are indicated.

center of Manila, a megacity (capital) of the Philippines [see Fig. 6(c)]. Fig. 6(e) and (g) shows monthly mean VISAI distributions for 04:45–05:15 UTC in April 2021. As previously described, the BPC-driven information gap cannot be filled even through long-term data accumulation due to the scanning mechanism of GEMS. In contrast, the band-shaped anomalies do not appear in the VISAI distributions derived using the gap-filled radiances [see Fig. 6(b), (d), (f), and (h)], supporting the effectiveness of the reconstruction algorithm.

Changes in the VISAI values affect aerosol type determination (see Section II-D). Fig. 7 illustrates the changes in aerosol types resulting from radiance reconstruction from August 2020 to July 2021 for GEMS pixels with the spatial indices of the BPC (1104–1134). Since the GEMS aerosol algorithm employs different lookup tables depending on aerosol types, alternations in aerosol types ultimately lead to changes in the final outputs: AOD, SSA, and ALH. After radiance reconstruction, the type classification results show that 47.2% of all ground pixels (1 369 665 pixels) are assigned the HAF type. Notably, 14.4% of these pixels are classified as dust without radiance reconstruction [see the left bar in Fig. 7]. The dust type is assigned to a relatively small number of ground pixels (106 786), yet it exhibits the highest type change rate; 44.9% of the pixels are classified as HAF without radiance reconstruction (see the middle bar in Fig. 7). The NA type, found at 49.1% of all ground pixels (1 424 589 pixels), shows a 15.3% masking rate without radiance reconstruction rather than being classified as other aerosol types (see the right bar in Fig. 7). These findings suggest that one significant outcome of radiance reconstruction in aerosol type determination is the redistribution between the HAF and dust aerosols. This result aligns with expectations, as the primary distinction between HAF and dust aerosols lies in their particle sizes, which are detectable through VISAI.

Fig. 8(a) shows the impact of the radiance reconstruction on the ALH retrieval for the spatial indices of the BPC (1104–1134) for one year of data from August 2020 to July 2021. The absolute changes in ALH values resulting from radiance construction have a standard deviation of 0.58 km. We note that 26.9% (15.0%) of data points exhibit changes exceeding 0.2 km (0.5 km), while 24.1% (12.8%) of data points show relative changes exceeding 20% (50%).

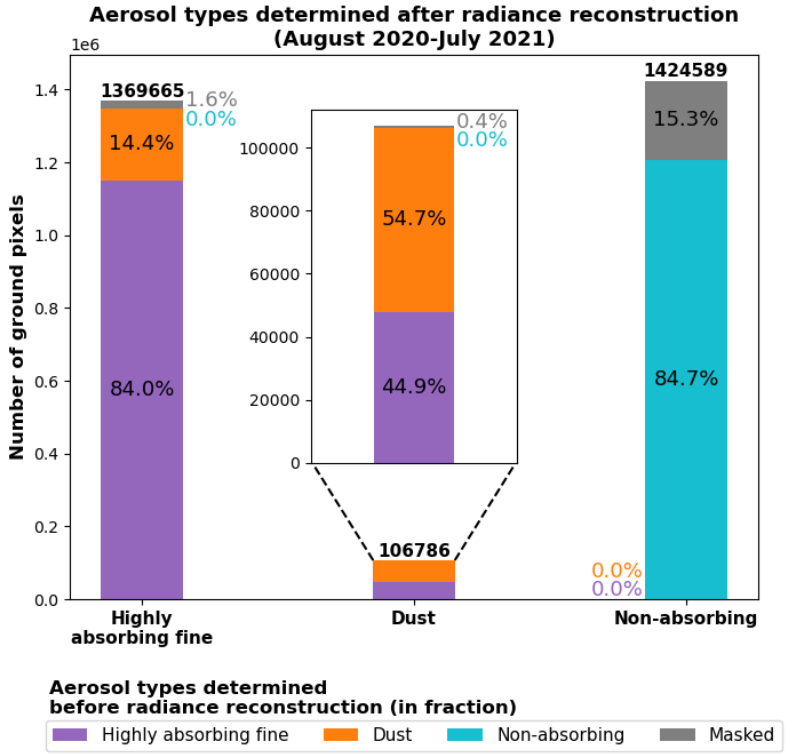

Fig. 7. Changes in aerosol type classifications resulting from radiance reconstruction for the spatial indices of the BPC (1104–1134) from August 2020 to July 2021. The total height of each of the three bars represents the number of GEMS ground pixels for each aerosol type determined after radiance reconstruction. The exact number of pixels is presented above each bar. Fractionally colored bars depict aerosol types determined without radiance reconstruction at the same GEMS pixels (in fraction). The fractions of pixels masked without radiance reconstruction are also indicated.

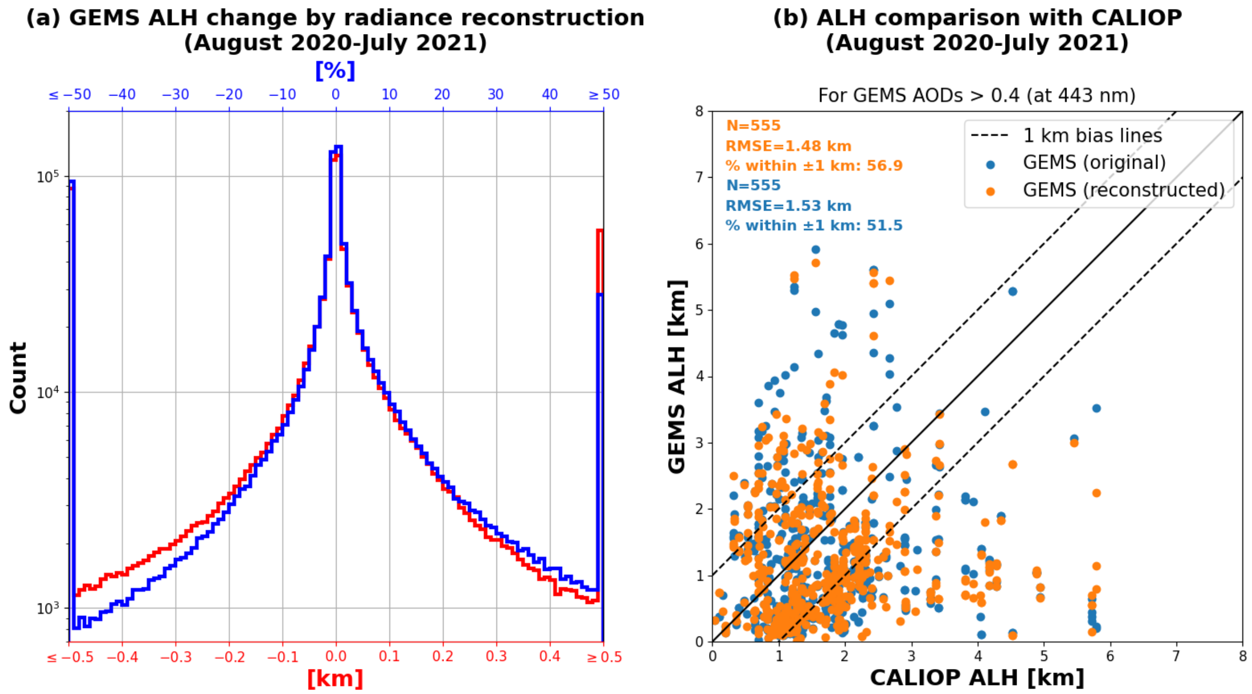

Fig. 8. Impacts of the radiance reconstruction on ALH retrieval for the BPC from August 2020 to July 2021. (a) Absolute and percentage changes in ALH values resulting from radiance reconstruction. (b) Intercomparison between the ALH retrievals from CALIOP and GEMS (for both with and without radiance reconstruction). The numbers of data points (N), RMSE, and the percentage of data points within the 1-km bias lines are indicated.

To verify whether the ALHs become more accurate after radiance reconstruction, we conduct intercomparison with retrievals from the Cloud-Aerosol Lidar with Orthogonal Polarization (CALIOP) (CAL_LID_L2_05kmAPro-Prov-V3-41 product) [45]. We calculate aerosol-weighted extinction height z_{ext}, referred to as CALIOP ALH hereafter, following

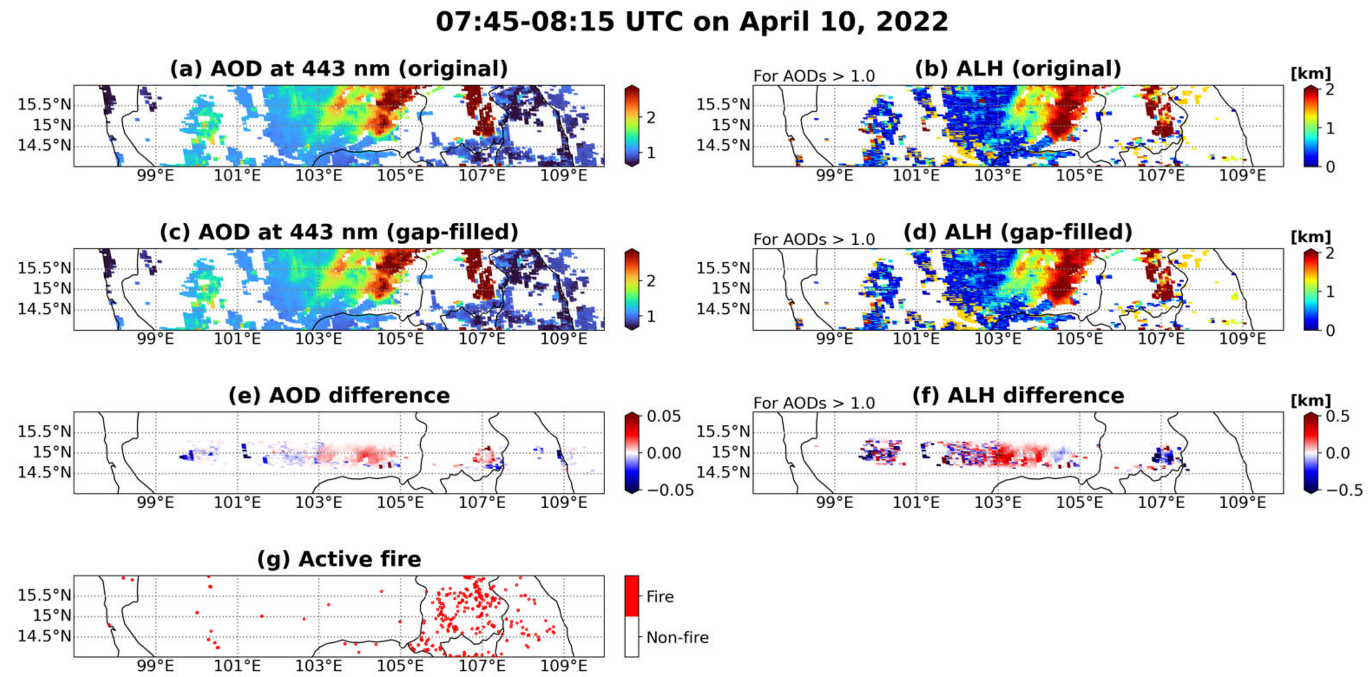

Fig. 9. Impacts of the radiance reconstruction on AOD and ALH retrievals at 07:45–08:15 UTC on April 10, 2022. The first row shows: (a) AOD at 443 nm and (b) ALH retrieved without radiance reconstruction. The second row presents: (c) AOD at 443 nm and (d) ALH retrieved with radiance reconstruction. Differences between the gap-filled and the original retrievals are presented for (e) AOD and (f) ALH. (g) Fire pixels obtained from the VIIRS VNP14A1 product at 1-km resolution for April 10, 2022. (b), (d), and (f) Only GEMS pixels with AODs >1.0. Aerosol retrievals over cloudy pixels are filtered out.

the approach of Koffi et al. [46]:

$$z_{\text{ext}} = \frac{\sum_{i=1}^{n} \beta_i z_i}{\sum_{i=1}^{n} \beta_i} \tag{12}$$

where β_i and z_i represent the extinction coefficient at 532 nm and altitude at vertical layer i, respectively, and n is the number of vertical layers. To achieve data co-location, we calculate the average of GEMS ALH values obtained from spatial indices 1104–1134 within a ±1-h window around each CALIOP measurement time from August 2020 to July 2021. We apply a radius of 0.05° for this averaging process. Given that the sensitivity of ALH retrieval depends on the AOD, only GEMS pixels with AODs >0.4 are used. In addition, ALH values outside the GEMS ALH lookup table coverage (0–6 km) are excluded for both GEMS and CALIOP. Fig. 8(b) presents the intercomparison results. The RMSE values before and after radiance reconstruction correspond to 1.53 and 1.48 km, respectively, with data points falling within the ±1-km bias lines at proportions of 51.5% and 56.9%. These statistics suggest that the radiance reconstruction leads to ALH retrievals with better quality.

In Mainland Southeast Asia, the GEMS BPC is spatially projected onto territories in Myanmar, Thailand, Laos, Cambodia, and Vietnam [see Fig. 6(a) and (e)]. This region, characterized by substantial mountainous terrain, experiences frequent biomass burning during dry seasons due to slash-and-burn agriculture practices [20], [21], [22]. Yin et al. [21] showed that AODs observed from MODIS in March and April were much higher than in the other months from 2011 to 2016. On April 10, 2022, GEMS observed high AOD values typically exceeding 1.0 in this region. Fig. 9(a) shows an enlarged view of the AOD field retrieved without radiance reconstruction from 03:45 to 04:15 UTC that day. To verify the presence of biomass burning, we extract fire mask data at 1-km horizontal spatial sampling from the daily Suomi National Polar-orbiting Partnership (Suomi NPP) NASA Visible Infrared Imaging Radiometer Suite (VIIRS) Thermal Anomalies/Fire (VNP14A1) Version 1 data product [47]. Fig. 9(g) displays the detection of fire pixels from the VIIRS satellite instrument throughout the region on April 10, suggesting the influence of biomass burning on the elevated AOD values. Consistent spatial patterns are found between AOD and fire over these areas in general, although aerosol retrievals over dense fire pixels in Laos and Vietnam are filtered out due to cloud contamination. The ALH values, derived without radiance reconstruction, are presented only for GEMS pixels having AODs >1.0 to focus on those with stronger aerosol signals, ensuring more reliable ALH retrievals [see Fig. 9(b)].

Fig. 9(e) and (f) shows the differences in AOD and ALH values induced by radiance reconstruction, respectively. The differences in AODs and ALHs range from −0.09 to 0.96 and from −3.89 to 1.35 km, respectively. The percentage differences in AOD values are found to be between −12.2% and 30.9%, while those in ALH values are from −99.9% to >100%. The ALH field is more significantly affected by the BPC than the AOD field as expected [see Section II-D]. The lower and upper limits of the ALH difference ranges are significantly higher than the typical values shown in Fig. 8(a). This example highlights that when analyzing severe pollution cases caused by biomass burning in Mainland Southeast Asia, using GEMS AOP retrievals without radiance reconstruction can lead to significant errors. In essence, implementing reconstruction enhances the investigation of biomass burning in this area, allowing for a more effective utilization of GEMS data.

IV. CONCLUSION

The bad-pixel radiances from the operational GEMS Level-1 data lower the quality of Level-2 products. Specifically, the bad pixels of interest in this study lead to band-shaped anomalies in aerosol retrievals, encompassing the entire field of regard in the east–west direction at ∼14.4–16.1°N. These anomalies obstruct continuous urban-scale air quality monitoring over India, Myanmar, Thailand, Laos, Vietnam, and the Philippines.

The reason aerosol retrievals are particularly affected is because the 490-nm channel used in the retrieval algorithm overlaps with the spectral range marked by the bad pixels (485–491 nm). Replacing the 490-nm channel with another wavelength requires re-optimization of algorithm parameters for the entire GEMS domain, including VISAI criteria for aerosol type determination and the measurement error covariance matrix for the OEM process. Without parameter re-optimization, a simple channel replacement would lead to biases in aerosol types, AODs, and ALHs. As the algorithm parameters have been optimized for the 490-nm channel, radiance reconstruction for 485–491 nm offers an efficient alternative to derive the spatially consistent aerosol retrievals over the entire GEMS domain.

This study proposes a robust method to reconstruct radiances, suitable for replacing the interpolated outputs provided from the currently operational Level-1 product. The reconstruction is performed based on linear spectral relationships between radiances from different wavelengths, determined by the Fraunhofer line structures and spectral patterns of optical depths. This approach assumes that a consistent spectral relationship can be found in radiances measured from different locations on the Earth's surface. Since this assumption does not hold true in practice, the reconstructed radiances necessarily have errors. However, since our ultimate objective is to offer reliable AOPs for latitudes around ∼14.4–16.1°N, it is worthwhile to proceed with the reconstruction as long as the errors in the reconstructed optical depths remain sufficiently small compared to AODs in the spectral range of 485–491 nm. It is noteworthy that we find the uncertainties in reconstructed optical depths to be ∼2 orders of magnitude smaller than typical AOD values within this spectral range. Also, the reconstructed Fraunhofer lines show consistent spectral structures with those from TROPOMI.

Theoretically, the radiance reconstruction method proposed in this study can be applied to the other two defect areas on the GEMS CCD. However, given their significantly wider spectral ranges (∼100 nm wide), careful implementation is recommended. Errors in our reconstruction method depend on the spatial variability in spectral patterns of optical depths. Therefore, the key to reliable application lies in constraining the spatial and spectral variabilities across the wide wavelength ranges. A spectrally recursive reconstruction may be a possible modification. Another consideration is comparing errors in reconstructed optical depths to the typical optical depths of the trace gas of interest.

In this study, for the circle-shaped defect area of interest, the reasonable spectral structures in the reconstructed radiances result in spatially continuous AOP data from GEMS. The reconstruction results demonstrate the successful rebuilding of physical distributions of VISAIs, leading to better aerosol type determinations. Furthermore, the reconstructed ALH values exhibit a better agreement with CALIOP observations. Finally, an analysis of a severe aerosol pollution episode demonstrates that the radiance reconstruction enhances the investigation of biomass burning in Mainland Southeast Asia, utilizing GEMS data more effectively. The GEMS aerosol product will include retrievals derived from reconstructed radiances, accompanied by a designated quality flag. Consequently, users will be able to make informed decisions regarding the utilization of these data based on their specific analyses and requirements.

ACKNOWLEDGMENT

The authors would like to acknowledge the free use of the TROPOMI S5P_L1B_RA_BD4_HiR product, the CALIOP CAL_LID_L2_05kmAPro-Prov-V3-41 product, and the VIIRS VNP14A1 product.

REFERENCES

[1] J. Kim et al., "New era of air quality monitoring from space: Geostationary Environment Monitoring Spectrometer (GEMS)," *Bull. Amer. Meteorological Soc.*, vol. 101, no. 1, pp. E1–E22, 2020.

[2] W. J. Choi et al., "Introducing the geostationary environment monitoring spectrometer," *IEEE J. Appl. Remote Sens.*, vol. 12, no. 4, Oct. 2018, Art. no. 044005.

[3] X. Li, H. Shen, L. Zhang, H. Zhang, and Q. Yuan, "Dead pixel completion of Aqua MODIS band 6 using a robust M-estimator multiregression," *IEEE Geosci. Remote Sens. Lett.*, vol. 11, no. 4, pp. 768–772, Apr. 2014.

[4] Q. Zhang, Q. Yuan, H. Shen, and L. Zhang, "A unified spatial–temporal–spectral learning framework for reconstructing missing data in remote sensing images," in *Proc. IEEE Int. Geosci. Remote Sens. Symp.*, Jul. 2018, pp. 4981–4984.

[5] Q. Zhang, Q. Yuan, C. Zeng, X. Li, and Y. Wei, "Missing data reconstruction in remote sensing image with a unified spatial–temporal–spectral deep convolutional neural network," *IEEE Trans. Geosci. Remote Sens.*, vol. 56, no. 8, pp. 4274–4288, Aug. 2018.

[6] Q. Cheng, Q. Yuan, M. K. Ng, H. Shen, and L. Zhang, "Missing data reconstruction for remote sensing images with weighted low-rank tensor model," *IEEE Access*, vol. 7, pp. 142339–142352, 2019.

[7] P. K. Charles et al., "Reconstruction of missing information in satellite imagery using STS-CNN," presented at the Int. Conf. Adv. Res. Innov. (ICARI), Jan. 2020.

[8] M. Shao, C. Wang, W. Zuo, and D. Meng, "Efficient pyramidal GAN for versatile missing data reconstruction in remote sensing images," *IEEE Trans. Geosci. Remote Sens.*, vol. 60, pp. 1–14, 2022, Art. no. 5626014.

[9] M. Shao, C. Wang, T. Wu, D. Meng, and J. Luo, "Context-based multiscale unified network for missing data reconstruction in remote sensing images," *IEEE Geosci. Remote Sens. Lett.*, vol. 19, pp. 1–5, 2022.

[10] Y. Zhou et al., "For-backward LSTM-based missing data reconstruction for time-series Landsat images," *GISci. Remote Sens.*, vol. 59, no. 1, pp. 410–430, Dec. 2022.

[11] Z. Tang, G. Amatulli, P. K. E. Pellikka, and J. Heiskanen, "Spectral temporal information for missing data reconstruction (STIMDR) of Landsat reflectance time series," *Remote Sens.*, vol. 14, no. 1, p. 172, Dec. 2021.

[12] B. Wang, J. Bao, S. Wang, H. Wang, and Q. Sheng, "Improved line tracing methods for removal of bad streaks noise in CCD line array image—A case study with GF-1 images," *Sensors*, vol. 17, no. 4, p. 935, Apr. 2017.

[13] F. N. Fritsch and R. E. Carlson, "Monotone piecewise cubic interpolation," *SIAM J. Numer. Anal.*, vol. 17, no. 2, pp. 238–246, Apr. 1980.

[14] Y. Lee, M.-H. Ahn, M. Kang, and M. Eo, "Spectral replacement using machine learning methods for continuous mapping of the geostationary environment monitoring spectrometer (GEMS)," *Atmos. Meas. Techn.*, vol. 16, no. 1, pp. 153–168, Jan. 2023.

[15] J. Kim et al. (Apr. 2020). *Geostationary Environment Monitoring Spectrometer (GEMS) Algorithm Theoretical Basis Document: Aerosol Retrieval Algorithm*. Environmental Satellite Center, National Institute of Environment Research, Ministry of Environment. [Online]. Available: https://nesc.nier.go.kr/en/html/satellite/doc/doc.do

[16] Y. Cho et al., "First atmospheric aerosol monitoring results from Geostationary Environment Monitoring Spectrometer (GEMS) over Asia," *Atmos. Meas. Techn. Discuss.*, vol. 2023, pp. 1–29, Oct. 2023.

[17] H. D. Alas et al., "Spatial characterization of black carbon mass concentration in the atmosphere of a Southeast Asian megacity: An air quality case study for metro Manila, Philippines," *Aerosol Air Quality Res.*, vol. 18, no. 9, pp. 2301–2317, 2018.

[18] P. K. Hopke et al., "Urban air quality in the Asian region," *Sci. Total Environ.*, vol. 404, no. 1, pp. 103–112, 2008.

[19] L. Tunisson et al., "From transfer to knowledge co-production: A transdisciplinary research approach to reduce black carbon emissions in metro Manila, Philippines," *Sustainability*, vol. 12, no. 23, Dec. 2020, Art. no. 10043.

[20] K. Huang et al., "Impact assessment of biomass burning on air quality in Southeast and east Asia during BASE-ASIA," *Atmos. Environ.*, vol. 78, pp. 291–302, Oct. 2013.

[21] S. Yin, X. Wang, X. Zhang, M. Guo, M. Miura, and Y. Xiao, "Influence of biomass burning on local air pollution in Mainland Southeast Asia from 2001 to 2016," *Environ. Pollut.*, vol. 254, Nov. 2019, Art. no. 112949.

[22] S. Yin, "Biomass burning spatiotemporal variations over south and Southeast Asia," *Environ. Int.*, vol. 145, Dec. 2020, Art. no. 106153.

[23] H. Lee et al. (Apr. 2020). *Geostationary Environment Monitoring Spectrometer (GEMS) Algorithm Theoretical Basis Document: NO_2 Retrieval Algorithm*. Environmental Satellite Center, National Institute of Environment Research, Ministry of Environment. [Online]. Available: https://nesc.nier.go.kr/en/html/satellite/doc/doc.do

[24] H. Lee and J. Yang. (Apr. 2020). *Geostationary Environment Monitoring Spectrometer (GEMS) Algorithm Theoretical Basis Document: SO_2 Retrieval Algorithm*. Environmental Satellite Center, National Institute of Environment Research, Ministry of Environment. [Online]. Available: https://nesc.nier.go.kr/en/html/satellite/doc/doc.do

[25] J. Kim and H. Lee. (May 2020). *Geostationary Environment Monitoring Spectrometer (GEMS) Algorithm Theoretical Basis Document: UV Index Retrieval Algorithm*. Environmental Satellite Center, National Institute of Environment Research, Ministry of Environment. [Online]. Available: https://nesc.nier.go.kr/en/html/satellite/doc/doc.do

[26] S. J. Lee et al., "Introduction on the products and the quality management plans for GOCI-II," *Korean J. Remote Sens.*, vol. 37, no. 5, pp. 1245–1257, 2021.

[27] S. Lee et al., "Retrieval of aerosol optical properties from GOCI-II observations: Continuation of long-term geostationary aerosol monitoring over east Asia," *Sci. Total Environ.*, vol. 903, Dec. 2023, Art. no. 166504.

[28] S. R. Aliwell et al., "Analysis for BrO in zenith-sky spectra: An intercomparison exercise for analysis improvement," *J. Geophys. Res., Atmos.*, vol. 107, no. D14, p. 4199, Jul. 2002.

[29] G. Kirchhoff, "Ueber die Fraunhofer'schen Linien," in *(On Fraunhofer's Lines), Monatsbericht der Königlichen Preussische Akademie der Wissenschaften Zu Berlin (Monthly Report of the Royal Prussian Academy of Sciences in Berlin)*. Berlin, Germany: Royal Prussian Academy of Sciences, 1859, pp. 662–665.

[30] M. Kang, M.-H. Ahn, X. Liu, U. Jeong, and J. Kim, "Spectral calibration algorithm for the geostationary environment monitoring spectrometer (GEMS)," *Remote Sens.*, vol. 12, no. 17, p. 2846, Sep. 2020.

[31] K. Chance, "Analysis of BrO measurements from the global ozone monitoring experiment," *Geophys. Res. Lett.*, vol. 25, no. 17, pp. 3335–3338, Sep. 1998.

[32] U. Platt, "Differential optical absorption spectroscopy (DOAS)," in *Air Monitoring by Spectroscopic Techniques*, vol. 127, M. W. Sigrist, Ed. New York, NY, USA: Wiley, 1994, pp. 27–84.

[33] G. Gonzalez Abad et al., "Five decades observing Earth's atmospheric trace gases using ultraviolet and visible backscatter solar radiation from space," *J. Quant. Spectrosc. Radiat. Transf.*, vol. 238, Nov. 2019, Art. no. 106478.

[34] M. Kim et al., "Optimal estimation-based algorithm to retrieve aerosol optical properties for GEMS measurements over Asia," *Remote Sens.*, vol. 10, no. 2, p. 162, Jan. 2018.

[35] S. Go et al., "Synergistic use of hyperspectral UV-visible OMI and broadband meteorological imager MODIS data for a merged aerosol product," *Remote Sens.*, vol. 12, no. 23, p. 3987, Dec. 2020.

[36] O. Torres, P. K. Bhartia, J. R. Herman, A. Sinyuk, P. Ginoux, and B. Holben, "A long-term record of aerosol optical depth from TOMS observations and comparison to AERONET measurements," *J. Atmos. Sci.*, vol. 59, no. 3, pp. 398–413, Feb. 2002.

[37] C. D. Rodgers, *Inverse Methods for Atmospheric Sounding: Theory and Practice, Series on Atmospheric, Oceanic, and Planetary Physics*, vol. 2. Singapore: World Scientific, 2002.

[38] O. Torres, P. K. Bhartia, J. R. Herman, Z. Ahmad, and J. Gleason, "Derivation of aerosol properties from satellite measurements of backscattered ultraviolet radiation: Theoretical basis," *J. Geophys. Res., Atmos.*, vol. 103, no. D14, pp. 17099–17110, Jul. 1998.

[39] R. Spurr, "VLIDORT: A linearized pseudo-spherical vector discrete ordinate radiative transfer code for forward model and retrieval studies in multilayer multiple scattering media," *J. Quant. Spectrosc. Radiat. Transf.*, vol. 102, pp. 316–342, Nov. 2006.

[40] S. S. Park, J. Kim, H. Lee, O. Torres, K.-M. Lee, and S. D. Lee, "Utilization of O4 slant column density to derive aerosol layer height from a space-borne UV–visible hyperspectral sensor: Sensitivity and case study," *Atmos. Chem. Phys.*, vol. 16, no. 4, pp. 1987–2006, Feb. 2016.

[41] W. Choi et al., "Effects of spatiotemporal o4 column densities and temperature-dependent o4 absorption cross-section on an aerosol effective height retrieval algorithm using the o4 air mass factor from the ozone monitoring instrument," *Remote Sens. Environ.*, vol. 229, pp. 223–233, Aug. 2019.

[42] J. P. Veefkind et al., "TROPOMI on the ESA Sentinel-5 precursor: A GMES mission for global observations of the atmospheric composition for climate, air quality and ozone layer applications," *Remote Sens. Environ.*, vol. 120, pp. 70–83, May 2012.

[43] *Sentinel-5P TROPOMI L1B Radiance Product Band 4 (UVIS Detector) 5.5km x 3.5km*, ESA and KNMI, GES DISC, Greenbelt, MD, USA, 2019, doi: 10.5067/SENTINEL5P/S5P_L1B_RA_BD4_HiR.1.

[44] G. Chander, T. J. Hewison, N. Fox, X. Wu, X. Xiong, and W. J. Blackwell, "Overview of intercalibration of satellite instruments," *IEEE Trans. Geosci. Remote Sens.*, vol. 51, no. 3, pp. 1056–1080, Mar. 2013.

[45] D. M. Winker, M. A. Vaughan, A. Omar, Y. Hu, and K. A. Powell, "Overview of the CALIPSO mission and CALIOP data processing algorithms," *J. Atmos. Ocean. Technol.*, vol. 26, no. 11, pp. 2310–2323, 2009.

[46] B. Koffi et al., "Application of the CALIOP layer product to evaluate the vertical distribution of aerosols estimated by global models: AeroCom phase i results," *J. Geophys. Res., Atmos.*, vol. 117, no. D10, p. D1, May 2012.

[47] W. Schroeder and L. Giglio, *VIIRS/NPP thermal anomalies/fire daily L3 global 1km SIN grid V001*. Sioux Falls, South Dakota: NASA EOSDIS Land Processes Distributed Active Archive Center, 2018, doi: 10.5067/VIIRS/VNP14A1.001.

Heesung Chong received the B.S. degree in chemical and biomolecular engineering and the Ph.D. degree in atmospheric sciences from Yonsei University, Seoul, South Korea, in 2015 and 2021, respectively.

He is currently a Post-Doctoral Researcher with the Center for Astrophysics | Harvard & Smithsonian, Cambridge, MA, USA. His primary research interests lie in the retrieval of trace gas concentrations in the Earth's atmosphere from remote sensing measurements and in the characterization and calibration of satellite instruments. He is currently a Science Team Member of the Tropospheric Emissions: Monitoring of Pollution (TEMPO) mission.

Won-Jin Lee (Member, IEEE) received the M.S. and Ph.D. degrees in geoinformatics from the University of Seoul, Seoul, South Korea, in 2010 and 2015, respectively.

He is currently a Senior Researcher with the Environmental Satellite Center, National Institute of Environmental Research, Incheon, South Korea. His research interests include the estimation and correction of InSAR processing and performance improvements of surface deformation measurement using multitemporal InSAR (MTInSAR) techniques. Recently, he has been focusing on the development of Geostationary Environment Monitoring Spectrometer (GEMS) algorithm and application. Also, the InSAR method to assess and predict risks associated with geophysical hazards.

Hyung-Sup Jung (Member, IEEE) received the M.S. degree in geophysics and the Ph.D. degree in remote sensing from Yonsei University, Seoul, South Korea, in 1998 and 2007, respectively.

He is currently a Professor with the Department of Geoinfomatics, the University of Seoul, Seoul. His primary research interests cover the development of algorithms related to: 1) synthetic aperture radar (SAR), SAR interferometry (InSAR), multiple-aperture InSAR (MAI), and multitemporal InSAR (MTInSAR); 2) automated geometric correction of multisensor images; and 3) multisensor image processing and fusion, thermal remote sensing, and multitemporal optical and thermal sensing. He has been developing algorithms for remote sensing applications related to: 1) 3-D deformation mapping by combining MAI and InSAR; 2) 2-D surface velocity estimation by combining MAI and along-track interferometry (ATI); 3) MAI-based ionospheric correction of radar interferograms; 4) multisensor fusion by the integration of optic and SAR, SAR and thermal, and optic and thermal images; 5) automated geometric correction for optic and SAR images; and 6) Earth's surface variation monitoring, such as urban subsidence monitoring, glacier monitoring, volcano monitoring, deforestation monitoring, forest mapping, forest fire mapping, and snow depth estimation.

Yeseul Cho received the B.S. and Ph.D. degrees in atmospheric sciences from Yonsei University, Seoul, South Korea, in 2018 and 2024, respectively.

She currently holds a post-doctoral position with the Department of Atmospheric Sciences, Yonsei University. Her research interests include the development of Geostationary Environment Monitoring Spectrometer (GEMS) aerosol retrieval algorithm and the remote sensing for aerosols and trace gases, including air pollutants and greenhouse gases.

Jhoon Kim (Member, IEEE) received the B.S. degree in atmospheric sciences from Seoul National University, Seoul, South Korea, in 1986, and the Ph.D. degree in atmospheric and space sciences from the University of Michigan, Ann Arbor, MI, USA, in 1991.

He was a Yonsei Lee Youn Jae Fellow Professor of atmospheric science and has dedicated his career to the study of remote sensing for aerosols and trace gases, including air pollutants and greenhouse gases. Prior to his role at Yonsei University, he held the position of Principal Researcher at Korea Aerospace Research Institute, Daejeon, South Korea. He is the Principal Investigator (P.I.) of GEMS, the first satellite instrument for air quality monitoring from geostationary earth orbit (GEO) at unprecedented spatiotemporal resolution. He is also a member of the Committee on Earth Observation Satellites (CEOS) AC-VC, where he contributes to the establishment of a coordinated GEO constellation for global air quality observation. He served as the Director for the establishment of Particulate Matter Research Institute, Samsung Advanced Institute of Technology (SAIT), Suwon, South Korea. He has authored over 220 articles.

Dr. Kim serves as a Guest Editor for Atmospheric Measurement Technique. He is a fellow of the Korean Academy of Science and Technology (KAST).

Gonzalo González Abad received the B.Sc. degree in physics from the Universidad de Valencia, Valencia, Spain, in 2008, and the Ph.D. degree in chemistry from the University of York, York, U.K., in 2012.

He is currently a Physicist at the Center for Astrophysics | Harvard & Smithsonian, Cambridge, MA, USA. His main research interest is the development of trace gas retrieval algorithms applicable to observations by spaceborne ultraviolet and visible solar light backscattered spectrometers. He leads the development of Tropospheric Emissions: Monitoring of Pollution (TEMPO) satellite instrument formaldehyde retrievals and is a member of the Atmospheric Composition Instrument (ACX) science team.